SIMULATION OF COMPLEX FLUIDS AND SOFT MATERIALS USING STOCHASTIC EULERIAN LAGRANGIAN METHODS WITH SHEAR BOUNDARY CONDITIONS

PAUL J. ATZBERGER *

Abstract. We introduce computational methods for rheological studies of soft materials and complex fluids. The approach allows for investigations of the roles played by the microstructure interactions and kinetics and by the dynamics of the fluid. The approach takes into account consistently the elastic mechanics of the microstructures, hydrodynamics, and thermal fluctuations. To study rheological responses to shear, generalized periodic boundary conditions are developed. These impose a specified rate of shear on the fluid and microstructures only at the boundaries of the unit cell. A number of challenges arise in practice. This includes discontinuities in the fluid equations at the boundary, complications in determining appropriate stochastic driving fields to account for thermal fluctuations, and the development of consistent discretizations for use in simulations. We present stochastic numerical methods which address each of these issues. To demonstrate how the methods can be used in practice, we present results for a few specific applications. This includes the study of shear thinning of a polymeric fluid, the study of complex moduli for the oscillatory responses of a polymerized lipid vesicle, and the study of aging of the shear viscosity of a gel-like material.

Key words. Statistical Mechanics, Complex Fluids, Soft Materials, Stochastic Eulerian Lagrangian Methods, SELM, Stochastic Immersed Boundary Methods, SIB, Fluctuating Hydrodynamics, Fluid-Structure Coupling, Polymeric Fluid, FENE, Vesicles, Gels.

Last update to manuscript was on October 5, 2010; 9:36pm.

1. Introduction. Complex fluids and soft materials exhibit rich properties owing to the distinct organization and kinetics of microstructures comprising the material. These materials include liquid crystals, colloidal suspensions, gels, lipids, and emulsions [30, 21, 35, 19, 13, 11, 36]. A central challenge is to understand how macroscopic properties arise from the organization and kinetics of the microstructures in response to stresses. This is made challenging by a number of issues. One important issue concerns the characteristic energy scales of the interactions between the microstructures which is often comparable to thermal energy. As a consequence, important roles are played by thermal fluctuations and entropic effects. This has the potential to yield subtle phenomena dependent on the temperature [26, 13, 9]. Another issue arises from the microstructure mechanics and interactions that often have features which span a wide range of length scales and time scales [19, 26]. To obtain tractable models for analysis and simulation, this presents the challenge of introducing approximations while formulating descriptions which still retain essential microscopic features of the material. Additional issues arise for many biological materials of interest. For these materials the microstructures are often no longer passive and may exert active forces. These features present challenges to modeling and simulation requiring methods which can account for active microstructure mechanics, hydrodynamically driven transport, and the roles played both by fluctuations induced by the active forces and by thermal fluctuations [12, 28, 32].

We present computational methods which address these issues. Our approach for modeling and simulating complex fluids and soft materials is discussed in Section 2. To study the rheological responses to shear, we develop generalized periodic boundary conditions which are discussed in Section 2. To work with this formulation, we develop stochastic numerical methods in Section 4. To demonstrate how the methods work in practice, we present results for a few specific applications in Section 6. We discuss the shear thinning of a polymeric fluid in Section 6.1. We investigate the complex moduli for the oscillatory responses of a

polymerized lipid vesicle in Section 6.2. We study the aging of the shear viscosity of a gel-like material in Section 6.3.

In summary, the computational methods allow for investigations of diverse models and phenomena associated with complex fluids and soft materials. The methods allow for simulation studies that take into account the roles played by the material microstructure, elastic mechanics, hydrodynamics, and thermal fluctuations.

2. Stochastic Eulerian Lagrangian Method. To study for complex fluids and soft materials the dynamics of the microstructures and the solvent fluid, we use a variant of the Stochastic Eulerian Lagrangian Method, abbreviated SELM [4]. As is rather natural for such systems, the microstructures will be described in a Lagrangian frame of reference while the fluid dynamics will be described in an Eulerian frame of reference. To obtain models which are tractable for numerical methods, approximations are introduced when coupling these descriptions. The SELM formalism provides a set of general principles for developing such approximate descriptions and for incorporating stochastic driving fields to account for thermal fluctuations.

For studies of complex fluids and soft materials we will extend the SELM approach in a few important ways. To account for shearing of the material, we introduce generalized periodic boundary conditions. To describe the fluid dynamics and handle discontinuities on the unit cell boundary, we work with fluid equations in a non-Eulerian moving frame of reference. To couple the description of the fluid and microstructures we make use of time dependent discretizations and coupling operators. We now discuss this approach in more detail.

The stochastic dynamics of the solvent fluid and microstructures are modeled by

$$(2.1) \qquad \rho \frac{d\mathbf{u}}{dt} = \mu \Delta \mathbf{u} - \nabla p + \Lambda[-\nabla_{\mathbf{X}}\Phi(\mathbf{X})] + (\nabla_{\mathbf{X}} \cdot \Lambda)\, k_B T + \mathbf{g}_{\mathrm{thm}}$$

$$(2.2) \qquad \nabla \cdot \mathbf{u} = 0$$

$$(2.3) \qquad \frac{d\mathbf{X}}{dt} = \Gamma \mathbf{u}$$

$$(2.4) \qquad \langle \mathbf{g}_{\mathrm{thm}}(s)\mathbf{g}_{\mathrm{thm}}^{T}(t)\rangle = -\,(2k_B T)\,\mu \Delta\, \delta(t - s).$$

The $\mathbf{u}$ denotes the fluid velocity and $\mathbf{X}$ the microstructure configurations. The potential energy of the microstructures is given by $\Phi[\mathbf{X}]$. It is assumed throughout that to a good approximation the solvent fluid can be treated as incompressible with Newtonian stresses [1, 8]. The $\mathbf{u}$ denotes the fluid velocity, ρ denotes the uniform fluid density, μ the dynamic fluid viscosity, and p the fluid pressure. To account for thermal fluctuations, we introduce a stochastic driving field $\mathbf{g}_{\mathrm{thm}}$ which is assumed to be a Gaussian process with mean zero and δ-correlation in time. The notation $\mathbf{g}\mathbf{h}^{T}$ should be interpreted as a tensor product and is meant to suggest an analogue with the outer-product which arises in the discrete setting.

The linear operators Γ and Λ model the fluid-structure coupling. The linear operators are assumed to have dependence only on the configuration degrees of freedom and time $\Gamma = \Gamma[\mathbf{X}, t]$, $\Lambda = \Lambda[\mathbf{X}, t]$. To ensure the coupling conserves energy in the inviscid and zero temperature limit, the following adjoint condition is imposed [4]

$$(2.5) \qquad \int_{\mathcal{S}} (\Gamma \mathbf{u})(\mathbf{s}) \cdot \mathbf{v}(\mathbf{s}) d\mathbf{s} = \int_{\Omega} \mathbf{u}(\mathbf{x}) \cdot (\Lambda \mathbf{v})(\mathbf{x}) d\mathbf{x}.$$

This is required to hold for any $\mathbf{u}$ and $\mathbf{v}$. The $\mathcal{S}$ and Ω denote the spaces used to parameterize respectively the microstructure configurations and the fluid. We denote such an adjoint by $\Lambda = \Gamma^{\dagger}$ or $\Gamma = \Lambda^{\dagger}$. A specific form for the coupling operators will be given in Section 4.3.

It should be mentioned that in general the thermal fluctuations induce significant irregularity in the velocity field $\mathbf{u}$. In fact, the $\mathbf{u}$ is not defined in a point-wise sense but only in terms of a generalized function (distribution) [29]. As a consequence, some care must be taken in the treatment of the material derivative $d\mathbf{u}/dt = \partial \mathbf{u}/\partial t + \mathbf{u} \cdot \nabla \mathbf{u}$, see discussion in [4]. For our present purposes, and to avoid these technical issues, we only consider here
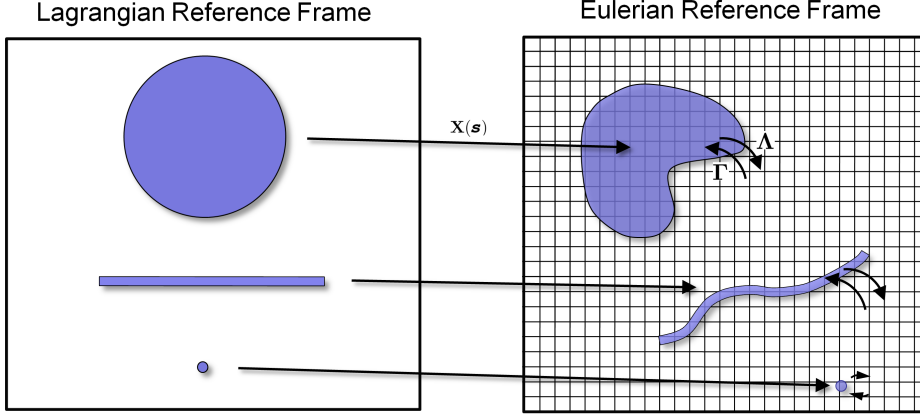
FIG. 2.1. *The description of the fluid-structure system utilizes both Eulerian and Lagrangian reference frames. The structure mechanics are often most naturally described using a Lagrangian reference frame. The fluid mechanics are often most naturally described using an Eulerian reference frame. The mapping* $\mathbf{X}(\mathbf{s})$ *relates the Lagrangian reference frame to the Eulerian reference frame. The operator* Γ *prescribes how structures are to be coupled to the fluid. The operator* Λ *prescribes how the fluid is to be coupled to the structures. A variety of fluid-structure interactions can be represented in this way. This includes rigid and deformable bodies, membrane structures, polymeric structures, or point particles.*

models that use the time-dependent Stokes equations with the linearized material derivative $d\mathbf{u}/dt = \partial\mathbf{u}/\partial t$.

3. Reformulation for Investigations of Shear Responses. To introduce shear we generalize the usual periodic boundary conditions. We are motivated by the approach introduced by Lees-Edwards for molecular dynamics methods [27, 15, 16]. In this work, the material is modeled by periodically repeating the unit cell of a molecular model. To simulate the material undergoing a shear deformation at a given rate, the periodic images are treated as shifting in time relative to the unit cell. This has the effect of modifying both the location of periodic images of molecules and their assigned velocities. This approach has some advantages over methods which enforce a strict affine-like deformation everywhere within the material body [17, 42, 22]. For the Lees-Edwards approach, the shear is imposed only at the boundaries allowing within the unit cell for the molecular interactions to determine the shear response, see Figure 3.1.

Motivated by this approach, we develop a corresponding methodology for the SELM approach. By considering the effect of shifting periodic images of the unit cell, we introduce the generalized periodic boundary conditions for the fluid velocity

$$(3.1) \qquad \mathbf{u}(x, y, L, t) = \mathbf{u}(x - vt, y, 0, t) + v\mathbf{e}_x.$$

To simplify the presentation, we only consider the case where a shear is imposed in the z-direction giving shear induced velocities in the x-direction. The other cases follow similarly. In our notation, the L is the side length of the periodic cell in the z-direction, $v = L\dot{\gamma}$ is the velocity of the top face of the unit cell relative to the bottom face, $\dot{\gamma}$ denotes the rate of shear deformation, and $\mathbf{e}_j$ is the standard unit vector in the jth direction. The interactions between microstructures of the system can be readily handled in the same manner as in the molecular dynamics simulation. This is done by shifting the location of any microstructure of a periodic image involved in an interaction, see Figure 3.1.

In practice, these boundary conditions present significant challenges for the numerical discretization of the fluid equations. The conditions introduce both a jump discontinuity at periodic boundaries and a shift. For uniform discretizations typically used for the unit
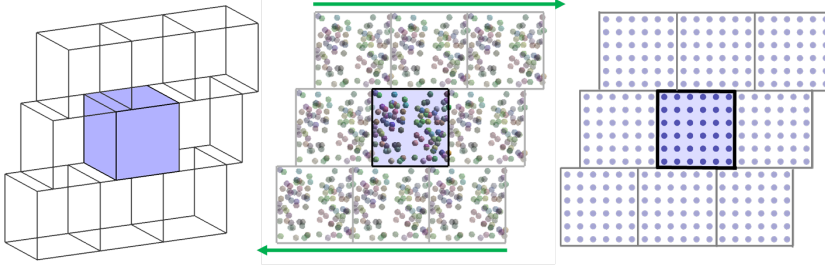
FIG. 3.1. *Discretization Mesh with Lees-Edwards Boundary Conditions Initial Formulation. The boundary conditions induce shear by shifting the periodic images of the unit cell, shown on the left and middle. For uniform discretizations of the unit cell this presents challenges since the mesh becomes misaligned at boundaries between the unit cell and the periodic images, shown on the right.*

cell, this results in significant misalignments of the nodes at the domain boundaries and a degradation in accuracy, see Figure 3.1. When incorporating stochastic driving fields to account for thermal fluctuations these issues are further compounded.

To address these issues, we reformulate the momentum equations in terms of a reference frame more naturally suited to the deformation of the material. This is achieved by letting $\mathbf{w}(\mathbf{q}, t) = \mathbf{u}(\phi(\mathbf{q}, t), t)$, where $\mathbf{q} = (q_1, q_2, q_3)$ parameterizes the deformed unit cell. The map from the moving coordinate frame to the fixed Eulerian coordinate frame is denoted by $\mathbf{x} = \phi(\mathbf{q})$ and given by $\phi(\mathbf{q}, t) = (q_1 + q_3 \dot\gamma t, q_2, q_3)$. The SELM equations 2.1– 2.4 in this reference frame are given by

$$(3.2) \qquad \rho \frac{d\mathbf{w}^{(d)}}{dt} = \mu \tilde\nabla^2 \mathbf{w} - \nabla p + \Lambda[-\nabla_{\mathbf{X}} \Phi] + (\nabla_{\mathbf{X}} \cdot \Lambda) \, k_B T + \mathbf{J} + \mathbf{G}_{\mathrm{thm}}$$

$$(3.3) \qquad \nabla \cdot \mathbf{w} = \mathbf{e}_z^T \, \nabla \mathbf{w} \, \mathbf{e}_x \dot\gamma t + \mathbf{K}$$

$$(3.4) \qquad \frac{d\mathbf{X}}{dt} = \Gamma \mathbf{w}$$

$$(3.5) \qquad \langle \mathbf{G}_{\mathrm{thm}}(s) \mathbf{G}_{\mathrm{thm}}^T(t) \rangle = -\,(2k_B T) \, \mu \tilde\nabla^2 \, \delta(t - s).$$

The Laplacian of the velocity field under the change of variable is given by

$$(3.6) \qquad \left[\tilde\nabla^2 \mathbf{w} \right]^{(d)} = [\mathbf{e}_d - \delta_{d,3} \dot\gamma t \mathbf{e}_x]^T \, \nabla^2 \mathbf{w}^{(d)} \, [\mathbf{e}_d - \delta_{d,3} \dot\gamma t \mathbf{e}_x] \,.$$

In this reference frame the misalignment arising from the shear boundary conditions is removed. The boundary conditions for the reformulation become formally periodic boundary conditions

$$(3.7) \qquad \mathbf{w}(q_1, q_2, L, t) = \mathbf{w}(q_1, q_2, 0, t).$$

The jump discontinuities arising from the boundary condition 3.1 still remain but in the reformulation are now taken into account by introducing the terms $\mathbf{J}, \mathbf{K}$. The term $\mathbf{G}_{\mathrm{thm}}$ denotes the stochastic driving field accounting for thermal fluctuations in the moving frame of reference.

The $\mathbf{q} = (q_1, q_2, q_3)$ parameterizes the deformed unit cell, $\delta_{k,\ell}$ denotes the Kronecker δ-function, $\dot\gamma$ denotes the rate of the shear deformation, and $\mathbf{e}_i$ the standard basis vector in the ith direction with $i \in \{x, y, z\}$. In the notation the parenthesized superscript denotes a vector component. We also use the notational conventions

$$(3.8) \qquad [\nabla \mathbf{w}]_j^{(d)} = \frac{\partial \mathbf{w}^{(d)}}{\partial q_j}, \qquad\qquad [\nabla^2 \mathbf{w}]_{i,j}^{(d)} = \frac{\partial^2 \mathbf{w}^{(d)}}{\partial q_i \partial q_j}.$$
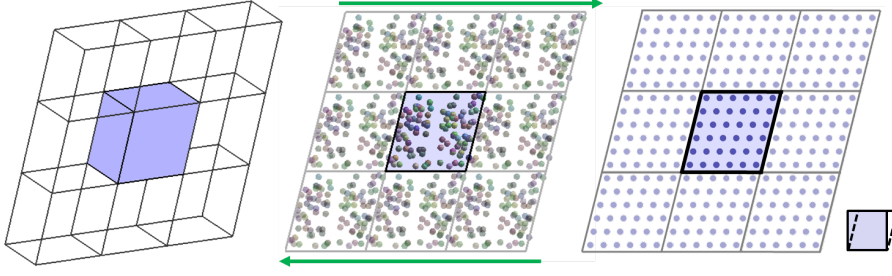
FIG. 3.2. *Discretization Mesh with Lees-Edwards Boundary Conditions Using a Moving Co-ordinate Frame. By discretizing the momentum equations in a moving coordinate frame a uniform discretization is obtained in which the mesh of the unit cell aligns with the mesh of the periodic images, shown on the left, middle, and right. The definition of the unit cell is changed over time from a cube to a sheared parallelepiped, shown on the far right on the bottom.*

4. Computational Methodology.

To use this approach in practice requires the development of numerical methods to approximate the stochastic differential equations. The development of discretizations encounter a few significant issues. One is to determine a proper discretization for the stochastic driving fields. Another is to develop efficient methods for generating the fields with the required covariance structure. Some additional challenges for the discretizations concern the development of operators which couple the microstructure and solvent fluid dynamics. A variety of methods could be used in practice to discretize the SELM formalism, such as Finite Difference Methods, Spectral Methods, and Finite Element Methods [20, 40, 39]. We present here discretizations based on Finite Difference Methods which address these issues.

The stochastic differential equations of SELM can exhibit significant stiffness. To help facilitate the development of efficient numerical methods for the SELM description, it will be useful to consider two distinct physical regimes. In the first we explicitly resolve the fluctuations and relaxation of the hydrodynamics. We refer to this as the Fluctuating Hydrodynamics Regime. In the second we treat the solvent fluid as having relaxed to a quasi-steady-state with respect the instantaneous configuration of the microstructures. We refer to this as the Overdamped Regime.

4.1. Numerical Methods for the Fluctuating Hydrodynamics Regime.

4.1.1. Semi-discretization.

To approximate the stochastic differential equations and to discretize the stochastic driving fields, we first consider a semi-discretization of the equations 3.2– 3.5. This is given by

$$(4.1) \qquad \rho \frac{d\mathbf{w}}{dt} = L(t)\mathbf{w} + \lambda + \Lambda[-\nabla_{\mathbf{X}}\Phi] + (\nabla_{\mathbf{X}} \cdot \Lambda)\, k_B T + \mathbf{J} + \mathbf{h}_{\mathrm{thm}}$$

$$(4.2) \qquad S(t) \cdot \mathbf{w} = \mathbf{K}$$

$$(4.3) \qquad \frac{d\mathbf{X}}{dt} = \Gamma\mathbf{w}.$$

We use for the discretized operators

$$(4.4) \qquad S(t) \cdot \mathbf{w} = D \cdot \mathbf{w} + \mathbf{e}_z^T\, G\mathbf{w}\, \mathbf{e}_x \dot{\gamma} t$$

$$(4.5) \qquad L(t)\mathbf{w} = [\mathbf{e}_d - \delta_{d,3}\dot{\gamma} t\mathbf{e}_x]^T\, A\mathbf{w}\, [\mathbf{e}_d - \delta_{d,3}\dot{\gamma} t\mathbf{e}_x]$$

where

$$(4.6) \qquad D \cdot \mathbf{w} = \sum_{d=1}^{3} \frac{\mathbf{w}^{(d)}(\mathbf{q} + \mathbf{e}_d) - \mathbf{w}^{(d)}(\mathbf{q} - \mathbf{e}_d)}{2\Delta x}$$

$$(4.7) \qquad [G\mathbf{w}]_{ij} = \frac{\mathbf{w}^{(i)}(\mathbf{q} + \mathbf{e}_j) - \mathbf{w}^{(i)}(\mathbf{q} - \mathbf{e}_j)}{2\Delta x}$$

and

$$(4.8) \qquad [A\mathbf{w}]_{ii} = \frac{\mathbf{w}^{(i)}(\mathbf{q} + \mathbf{e}_i) - 2\mathbf{w}^{(i)}(\mathbf{q}) + \mathbf{w}^{(i)}(\mathbf{q} - \mathbf{e}_i)}{\Delta x^2}$$

$$(4.9) \qquad [A\mathbf{w}]_{ij} = \frac{\mathbf{w}^{(d)}(\mathbf{q} + \mathbf{e}_i + \mathbf{e}_j) - \mathbf{w}^{(d)}(\mathbf{q} - \mathbf{e}_i + \mathbf{e}_j)}{4\Delta x^2}$$
$$- \frac{\mathbf{w}^{(d)}(\mathbf{q} + \mathbf{e}_i - \mathbf{e}_j) - \mathbf{w}^{(d)}(\mathbf{q} - \mathbf{e}_i - \mathbf{e}_j)}{4\Delta x^2}, \ i \neq j.$$

For the semi-discretized system we consider the energy

$$(4.10) \qquad E[\mathbf{w}, \mathbf{X}] = \frac{\rho}{2} \sum_{\mathbf{q}} |\mathbf{w}(\mathbf{q})|^2 \Delta x_{\mathbf{q}}^3 + \Phi[\mathbf{X}].$$

The first term is the total kinetic energy of the system. The second term is the potential energy of the microstructures.

For the discretized equations and energy, the $\mathbf{w}$ denotes the velocity field of the fluid on a uniform periodic lattice in the coordinates $\mathbf{q}$ with $\mathbf{w} \in \mathbb{R}^{3N}$. The N denotes the number of lattice sites. The $\mathbf{X}$ denotes a finite number of microstructure degrees of freedom with $\mathbf{X} \in \mathbb{R}^M$. As a consequence of the coordinate frame moving with the deformation of the unit cell, the discretized operators now have a direct dependence on time. The λ denotes a Lagrange multiplier used to impose the incompressibility condition 4.2 and will be discussed in more detail below.

To obtain the source terms $\mathbf{J}$, $\mathbf{K}$ for the discretized equations, we use the discretization stencils of the operators given in equations 4.1– 4.2. When the stencils weights are applied at the boundaries of the unit cell, the values at lattice sites crossing the boundary would use the modified image value $\mathbf{w_m} \pm \dot{\gamma}L$ under the boundary conditions 3.1. The use in the stencils of this modified lattice site value can be avoided by separating the contributions coming from the jump part of the boundary condition from the usual lattice site value of a periodic image. These contributions are given by the stencil weights multiplied by $\pm\dot{\gamma}L$ for any term crossing the boundary. When these are collected over all boundary mesh sites and terms on the right-hand side involving $\mathbf{w}$, we obtain the source terms $\mathbf{J}$, $\mathbf{K}$.

The incompressibility constraint for the solvent fluid is approximated in practice using the projection of a vector $\mathbf{v}^*$ to the sub-space $\{\mathbf{v} \in \mathbb{R}^{3N} \,|\, S(t) \cdot \mathbf{v} = 0\}$. We denote this projection operation by

$$(4.11) \qquad \mathbf{v} = \wp(t)\mathbf{v}^*.$$

The discretized incompressibility constraint is imposed by using the Lagrange multiplier

$$(4.12) \qquad \lambda = -(\mathcal{I} - \wp(t)) \left[L(t)\mathbf{w} + \Lambda[-\nabla_\mathbf{X}\Phi] + (\nabla_\mathbf{X} \cdot \Lambda)\, k_B T + \mathbf{J} + \mathbf{h}_{\mathrm{thm}} \right].$$

We remark that the incompressibility constraint is imposed exactly provided that $\mathbf{K}$ is independent of time. In practice, $\mathbf{K}$ is expected to have some dependence on time so that this approach results in an approximation in imposing the incompressibility constraint 4.2.

An important feature of the discretization for the SELM equations and incompressibility constraint is that the resulting operators are cyclic. This allows for Fast Fourier Transforms (FFTs) to be used in evaluating the action of the operators and in computing inverses. As a consequence, the projection operator can be computed efficiently with only $O(N \log(N))$ computational steps.

To obtain appropriate behaviors for the thermal fluctuations, it is important to develop stochastic driving fields which are tailored to the specific semi-discretization used. Another important issue is to develop methods for efficient generation of the stochastic fields. Once these issues are resolved, which is the subject of the next few sections, the semi-discretized

equations can be integrated in time using traditional methods for stochastic differential equations, such as the Euler-Maruyama Method or a Stochastic Runge-Kutta Method [24]. More sophisticated integrators in time can also be developed to cope with possible sources of stiffness [6].

4.1.2. Thermal Fluctuations. To account for thermal fluctuations, we introduce into the discretized equations a stochastic driving field. Given the highly irregular nature of the stochastic driving fields in the undiscretized equations 2.1– 2.4, formulating appropriate terms for the discretized equations must be done carefully. To obtain results consistent with statistical mechanics, we consider the relationship between the choice of stochastic driving field and the equilibrium fluctuations expected for the system. To simplify the discussion, we initially consider only the case when $\Phi = 0$ and neglect the $\mathbf{X}$ degrees of freedom. We then discuss how the results obtained apply to the more general case.

The statistical mechanics of the system requires equilibrium fluctuations which follow the Gibbs-Boltzmann distribution

$$(4.13) \qquad \Psi(\mathbf{w}, \mathbf{X}) = \frac{1}{Z} \exp\left[-E[\mathbf{w}, \mathbf{X}]/k_B T\right].$$

The Z is the normalization constant ensuring the probability integrates to one. The k_B is Boltzmann's constant and T is the temperature [37]. By considering the energy associated with the discretized system given in equation 4.10, we see that fluctuations of $\mathbf{w}$ are Gaussian under the Gibbs-Boltzmann distribution. This specific form of the energy along with the incompressibility constraint requires equilibrium fluctuations that have mean zero and covariance given by

$$(4.14) \qquad C = \langle \mathbf{w}\mathbf{w}^T \rangle = \frac{2}{3}\frac{k_B T}{\rho \Delta x^3}\mathcal{I}.$$

The factor of 2/3 arises from the incompressibility constraint. The stochastic driving field $\mathbf{h}_{\mathrm{thm}}$ introduced into the discretized equations is assumed to be a Gaussian process with mean zero and δ-correlation in time [18, 33]. Such processes can be expressed formally as

$$(4.15) \qquad \mathbf{h}_{\mathrm{thm}} = Q(t)\frac{d\mathbf{B}(t)}{dt}.$$

The $Q(t)$ denotes a linear operator and $\mathbf{B}(t)$ denotes a standard Brownian motion on $\mathbb{R}^{3N}$, see [33]. The covariance of this process is given by

$$(4.16) \qquad G(s, t) = \langle \mathbf{h}_{\mathrm{thm}}(s)\mathbf{h}_{\mathrm{thm}}(t)^T \rangle = Q(s)Q(t)^T \delta(t - s).$$

The discretized equations are linear in $\mathbf{w}$. As a consequence, the covariance of the equilibrium fluctuations and the covariance of the stochastic driving field are related by

$$(4.17) \qquad G(s, t) = -2\wp(t)L(t)C\delta(t - s).$$

This relation can be interpreted as a variant of the fluctuation-dissipation principle. We establish this relationship for systems having time dependent dissipative operators in Appendix A.

This gives the the stochastic driving field $\mathbf{h}_{\mathrm{thm}}$ tailored to the moving coordinate frame and the semi-discretized equations 4.1– 4.3. By considering the Fokker-Planck equations of the discretized system $(\mathbf{w}, \mathbf{X})$, this choice can be shown to yield stochastic dynamics which have the Gibbs-Boltzmann distribution invariant, see [4]. This shows the stochastic dynamics exhibit fluctuations consistent with equilibrium statistical mechanics. It should be mentioned, evaluating the appropriateness of this choice for the stochastic driving field also can be investigated by considering other properties, such as the dynamic structure factor of the stochastic dynamics that could be used to make comparisons with the undiscretized equations or with physical systems [14, 31]. Another important issue arising in practice is to develop computational methods for the efficient generation of the stochastic driving field. This is the subject of the next section.

4.1.3. Generation of Stochastic Driving Fields. To account for thermal fluctuations, we must generate each time step the Gaussian stochastic field with the covariance structure given by equation 4.17. In general, generating a Gaussian variate $\mathbf{h}$ with a prescribed covariance G is computationally expensive. A common approach is to generate standard normal variates $\boldsymbol{\xi}$ having covariance $\langle \boldsymbol{\xi}\boldsymbol{\xi}^T \rangle = I$. To obtain a correlated Gaussian a Cholesky factorization is often used to obtain $QQ^T = G$ and the Gaussian is generated using $\mathbf{h} = Q\boldsymbol{\xi}$. For $\mathbf{h} \in \mathbb{R}^N$, the Cholesky factorization has a cost of $O(N^3)$ computational steps and the generation of each variate through the matrix-vector multiplication has a cost of $O(N^2)$ computational steps. For the discretized equations N will typically be rather large making this approach prohibitive.

To generate the stochastic driving field more efficiently, we make use of specific properties of the discretization and FFTs. These properties include that $\mathbf{w}$ is periodic in the moving coordinate frame and that the discretized operators $L(t)$, C, and $\wp(t)$ are block diagonalizable in the Fourier basis (with blocks of small size). By working with the diagonalized form of each of the operators $L(t)$, C, and $\wp(t)$, a square-root $Q(t)$ of the operator $G(t)$ can be found in Fourier space. Given the sparse structure of $Q(t)$ in the Fourier space, the stochastic fields are generated using FFTs in $O(N\log(N))$ computational steps.

4.2. Numerical Methods for the Overdamped Regime. For many physical systems of interest, there are significant differences in the time scales associated with the hydrodynamic relaxation of the solvent fluid and the time scales associated with the diffusion of the microstructures an appreciable distance. For the fluctuating hydrodynamics regime this can result in significant stiffness in the stochastic differential equations.

For investigations of complex fluids and soft materials in which the relaxation of the hydrodynamics is not of primary interest, it is useful to introduce a reduced description removing this source of stiffness. In the limit of fluid dynamics which rapidly equilibrate given the instantaneous configuration of the microstructures we have the reduced equations,

$$(4.18) \qquad \frac{d\mathbf{X}}{dt} = H_{\text{SELM}}[-\nabla_{\mathbf{X}}\Phi(\mathbf{X})] + (\nabla_{\mathbf{X}} \cdot H_{\text{SELM}})k_B T + \mathbf{h}_{\text{thm}}$$

$$(4.19) \qquad H_{\text{SELM}} = \Gamma(-\wp L)^{-1}\Lambda$$

$$(4.20) \qquad \langle \mathbf{h}_{\text{thm}}(s)\mathbf{h}_{\text{thm}}^T(t) \rangle = (2k_B T)\, H_{\text{SELM}}\, \delta(t - s).$$

The $\wp$ denotes a projection operator imposing constraints, such as incompressibility. The adjoint property $\Lambda = \Gamma^\dagger$ and symmetry of $\wp L$ yields an operator H_{SELM} which is symmetric. The semi-discretization of these equations is obtained by using the discretized operators given in equations 4.4– 4.5. The thermal fluctuations are determined by the principle of detailed-balance and the requirement that the Gibbs-Boltzmann distribution be invariant under the stochastic dynamics, see [4]. The semi-discretized equations can be integrated in time using standard methods for stochastic differential equations [24]. A central challenge in using this approach in practice is the efficient generation of the stochastic driving field with the required covariance structure.

4.2.1. Generation of Stochastic Driving Fields. To use this description in practice requires efficient methods for generating the stochastic driving field with the covariance given in equation 4.20. For this purpose we express the covariance of the stochastic driving field as

$$(4.21) \qquad G = (2k_B T)H_{\text{SELM}} = (2k_B T)\left(\Gamma\wp(-L)^{-1}\wp^T\Gamma^T\right).$$

This makes use of $\Lambda = \Gamma^T$ and properties of the specific discretized operators L and $\wp$. In particular, commutativity $\wp L = L\wp$ and the projection operator properties $\wp^2 = \wp$, $\wp = \wp^T$. Let U be a factor so that $UU^T = -L^{-1}$. Using this factor we can express the covariance as

$$(4.22) \qquad G = \left(\sqrt{2k_B T}\Gamma\wp U\right)\left(\sqrt{2k_B T}\Gamma\wp U\right)^T.$$

From this expression a matrix square-root of G is readily obtained, $Q = \sqrt{2k_BT}\Gamma\wp U$.

We remark this is different than the Cholesky factor obtained for G which is required to be lower triangular [41, 38]. Obtaining such a factor by Cholesky factorization would cost $O(M^3)$, where M is the number of structure degrees of freedom. For the current discretization considered, the operators L and $\wp$ are block diagonalizable in Fourier space (with small blocks). This has the consequence that the action of the operators U and $\wp$ can be computed using FFTs with a cost of $O(N \log(N))$. The N is the number of lattice sites used to discretize L. The stochastic driving field is computed from $\mathbf{h} = Q\boldsymbol{\xi}$. This allows for the stochastic driving field to be generated in $O(N \log(N) + M)$ computational steps, assuming the action Γ can be compute in $O(M)$ steps. This is in contrast to using the often non-sparse matrix arising from Cholesky factorization which generates the stochastic field with a cost of $O(M^2)$. Other methods based on splittings or multigrid can also be utilized to efficiently generate stochastic fields with this required covariance structure or for discretizations on multilevel adaptive meshes, see [4, 2].

4.3. Operators for Coupling the Microstructures and Solvent Fluid. Many different operators could be used to couple the microstructure and solvent dynamics [4]. We will take an approach similar to the Stochastic Immersed Boundary Method [6, 34] and use the following specific form for the operators that couple the microstructures and solvent fluid

$$(4.23) \qquad [\Gamma\mathbf{u}](\mathbf{s}) = \int_\Omega \eta(\mathbf{y} - \mathbf{X}(\mathbf{s}))\mathbf{u}(\mathbf{y})d\mathbf{y}$$

$$(4.24) \qquad [\Lambda\mathbf{F}](\mathbf{y}) = \int_\mathcal{S} \mathbf{F}(\mathbf{s})\eta(\mathbf{y} - \mathbf{X}(\mathbf{s}))d\mathbf{s}.$$

The $\mathbf{F}$ denotes the force acting on the microstructures, which is typically given by $\mathbf{F} = -\nabla_\mathbf{X}\Phi$. The kernel function η is used to smooth the irregular velocity field and determines an effective hydrodynamic radius for the microstructures, see [4, 6] and Appendix B. It can be shown these operators satisfy the adjoint condition given by equation 2.5. This pair of operators has been successfully used in the past and extensive validation studies have been conducted to characterize how these operators represent hydrodynamic coupling [6, 3, 5, 4, 25, 10].

To couple the semi-discretized description of the solvent fluid and microstructures we use the discretized operators

$$(4.25) \qquad [\Gamma\mathbf{u}]^{[j]} = \sum_\mathbf{m} \eta(\mathbf{y_m} - \mathbf{X}^{[j]})\mathbf{u_m}\Delta y_\mathbf{m}^d$$

$$(4.26) \qquad [\Lambda\mathbf{F}]_\mathbf{m} = \sum_{j=1}^M \mathbf{F}^{[j]}(\mathbf{X})\eta(\mathbf{y_m} - \mathbf{X}^{[j]}).$$

It can be shown these operators satisfy an adjoint condition analogous to equation 2.5 for the semi-discretized equations 4.1– 4.3. More general discretized operators can also be used, see [4].

5. Estimating Macroscopic Stresses. An important issue in the study of complex fluids and soft materials is to relate microscopic features of the material to macroscopic properties. For this purpose, we develop estimators for an effective macroscopic stress tensor for the material. The stress tensor is estimated from the forces acting on the microstructures in a manner similar to that used in the Irving-Kirkwood-Kramer formulas [23, 13, 8, 9]. The contributions from the solvent fluid are assumed to be Newtonian throughout.

The stress tensor is estimated by considering cut-planes which divide the unit cell. A component of the stress tensor is estimated by considering the forces exerted by the material which lies above the cut-plane on the material which lies below the cut-plane. The totality of these forces is then divided by the area of the cut-plane. We average these estimates over all
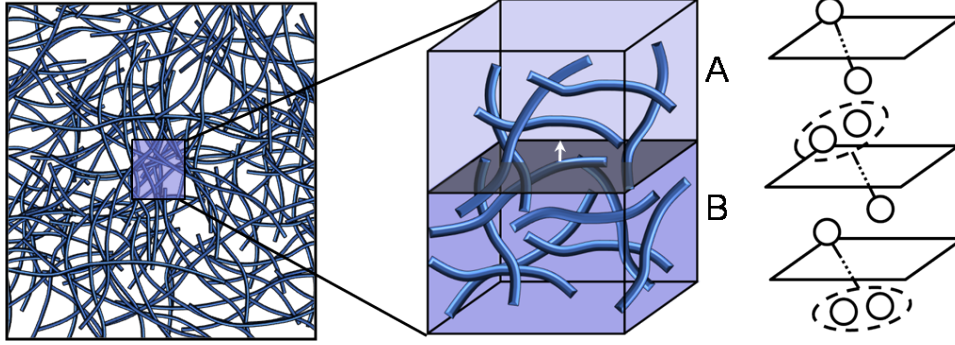
FIG. 5.1. *Estimating Macroscopic Stresses. The components of the stress tensor are estimated from microscopic interactions by considering cut-planes through the sample. The cut-plane divides the sample into two bodies labeled A and B, shown in the middle. The effective stress is given by the forces exerted by the material of body A on material of body B divided by the cut-plane area. For n-body interactions, contributions to the stress can arise in different ways. On the far right is shown for a given cut-plane the cases when two-body and three-body interactions make a contribution to the stress.*

possible cut-planes having a given normal to avoid sensitive dependence on the microstructure configuration, the n-body interactions, and the cut-plane location, see Figure 5.1.

To estimate the stress tensor, it is convenient to consider separately each of the different types of n-body interactions which occur between the microstructures, such as two-body bonding interactions or three-body bond-angle interactions. To estimate the contributions to the components of the stress tensor arising from a particular n-body interaction, we use

$$(5.1) \qquad \sigma_{\ell,z}^{(n)} = \frac{1}{L}\left\langle \int_a^b \Theta_{\ell,z}^{(n)}(\zeta)d\zeta \right\rangle.$$

The $L = b - a$ is the length of the unit-cell domain in the z-direction and $\langle \cdot \rangle$ denotes averaging over the ensemble. The $\Theta_{\ell,z}^{(n)}$ denotes the effective stress arising from the n-body interactions associated with a given stress plane and is defined by

$$(5.2) \qquad \Theta_{\ell,z}^{(n)}(\zeta) = \frac{1}{A} \sum_{\mathbf{q}\in\mathcal{Q}_n} \sum_{k=1}^{n-1}\sum_{j=1}^{k} \mathbf{f}_{\mathbf{q},j}^{(\ell)} \prod_{j=1}^{k} \mathcal{H}(\zeta - \mathbf{x}_{q_j}^{(z)}) \prod_{j=k+1}^{n} \mathcal{H}(\mathbf{x}_{q_j}^{(z)} - \zeta).$$

The $\mathcal{Q}_n$ is the set of n-tuple indices $\mathbf{q} = (q_1, \ldots, q_n)$ describing the n-body interactions of the system, $\mathbf{f}_{\mathbf{q},j}$ denotes the force acting on the jth particle of the interaction, and $\mathbf{x}_{q_j}$ denotes the jth particle involved in the interaction. As a matter of convention in the indexing $\mathbf{q}$, we require that $i \le j$ implies $\mathbf{x}_{q_i}^{(z)} \le \mathbf{x}_{q_j}^{(z)}$. This expression corresponds to a sum over all the forces exerted by particles of the material above the cross-section at $\zeta = z$ on the particles of the material below. Each term of the summation over $k = 1, \ldots, n-1$ corresponds to a specific number of particles of the n-body interaction lying below the cross-section at $\zeta = z$, see Figure 5.1.

This expression for estimating the stress tensor can be simplified by using the following identity

$$(5.3) \qquad \int_a^b \Pi_{j=1}^k \mathcal{H}(\zeta - \mathbf{x}_{q_j}^{(z)}) \cdot \Pi_{j=k+1}^n \mathcal{H}(\mathbf{x}_{q_j}^{(z)} - \zeta)d\zeta = \mathbf{x}_{q_{k+1}}^{*,(z)} - \mathbf{x}_{q_k}^{*,(z)}$$

where

$$(5.4) \qquad \mathbf{x}_{q_j}^{*,(z)} = \begin{cases} b, & \text{if } \mathbf{x}_{q_j}^{(z)} \ge b \\ \mathbf{x}_{q_j}^{(z)}, & \text{if } a \le \mathbf{x}_{q_j}^{(z)} \le b \\ a, & \text{if } \mathbf{x}_{q_j}^{(z)} \le a. \end{cases}$$

By integrating equation 5.2 and using the identity given in equation 5.3, we obtain

$$(5.5) \qquad \int_a^b \Theta_{(\ell),z}^{(n)}(\zeta)d\zeta = \frac{1}{A} \sum_{\mathbf{q} \in \mathcal{Q}_n} \sum_{k=1}^{n-1} \sum_{j=1}^{k} \mathbf{f}_{\mathbf{q},j}^{(\ell)} \cdot \left(\mathbf{x}_{q_{k+1}}^{*,(z)} - \mathbf{x}_{q_k}^{*,(z)} \right).$$

This can be further simplified by switching the order of summation of j and k and using the telescoping property of the summation over k. This gives the following estimate for the n-body contributions to the stress tensor

$$(5.6) \qquad \sigma_{\ell,z}^{(n)} = \frac{1}{AL} \sum_{\mathbf{q} \in \mathcal{Q}_n} \sum_{j=1}^{n-1} \left\langle \mathbf{f}_{\mathbf{q},j}^{(\ell)} \cdot \left(\mathbf{x}_{q_n}^{*,(z)} - \mathbf{x}_{q_j}^{*,(z)} \right) \right\rangle.$$

This is obtained by using equation 5.1 and equation 5.5.

To obtain the effective macroscopic stress tensor we sum over all n-body contributions to obtain

$$(5.7) \qquad \sigma_{\ell,z} = \sum_n \sigma_{\ell,z}^{(n)}.$$

This effective macroscopic stress tensor will be used to link the microscopic simulations to macroscopic material properties.

6. Applications. To demonstrate how the computational methods can be used to study the rheological behaviors of complex fluids and soft materials, we present a few specific applications. We investigate the shear thinning of a polymeric fluid in Section 6.1. We study the complex moduli for the oscillatory responses of a polymerized lipid vesicle in Section 6.2. We study the aging of the shear viscosity of a gel-like material in Section 6.3.

6.1. Application I: Shearing Thinning of a Polymeric Fluid. As a demonstration of the proposed computational methodology we consider a fluid with microstructures consisting of elastic polymers. The polymers are modeled as elastic dimers which have the FENE potential energy [9]

$$(6.1) \qquad \phi(r) = \frac{1}{2} K r_0^2 \log \left(1 - \left(\frac{r}{r_0} \right)^2 \right).$$

The K denotes the polymer stiffness, r denotes the length of extension of the dimer, and r_0 denotes the maximum permitted extension length. The configuration of a dimer will be represented using two degrees of freedom $\mathbf{X}_k^{(1)}$, $\mathbf{X}_k^{(2)}$ with the potential energy $\Phi(\mathbf{X}) = \sum_k \phi(|\mathbf{X}_k^{(2)} - \mathbf{X}_k^{(1)}|)$. The $\mathbf{X}$ denotes the composite vector over all dimers.

To study the rheology of the polymeric fluid, we consider the shear viscosity η_p and the first normal stress coefficient Ψ_1. These are defined as [8, 9]

$$(6.2) \qquad \eta_p = \sigma_p^{(s,v)}/\dot{\gamma}$$

$$(6.3) \qquad \Psi_1 = (\sigma_p^{(s,s)} - \sigma^{(v,v)})/\dot{\gamma}^2.$$

The $\dot{\gamma}$ is the rate of shear. In the notation, the superscript (s,v) indicates the tensor component with the index s corresponding to the direction of the shear gradient and the index v corresponding to the direction of the velocity induced by the shear. The contributions of the solvent fluid to the shear viscosity and normal stresses can be considered separately [9]. The solvent fluid is assumed to be Newtonian throughout so we only report the contributions arising from the elastic dimers.

From the simulations, we find there is a strong dependence on the rate of shear in the manifested shear viscosity and normal stress of the polymeric fluid, see Figure 6.1. This can be understood by considering the interplay between the thermal fluctuations and the shear stresses acting on the dimers. Since the dimers only resist stretching, they exert forces
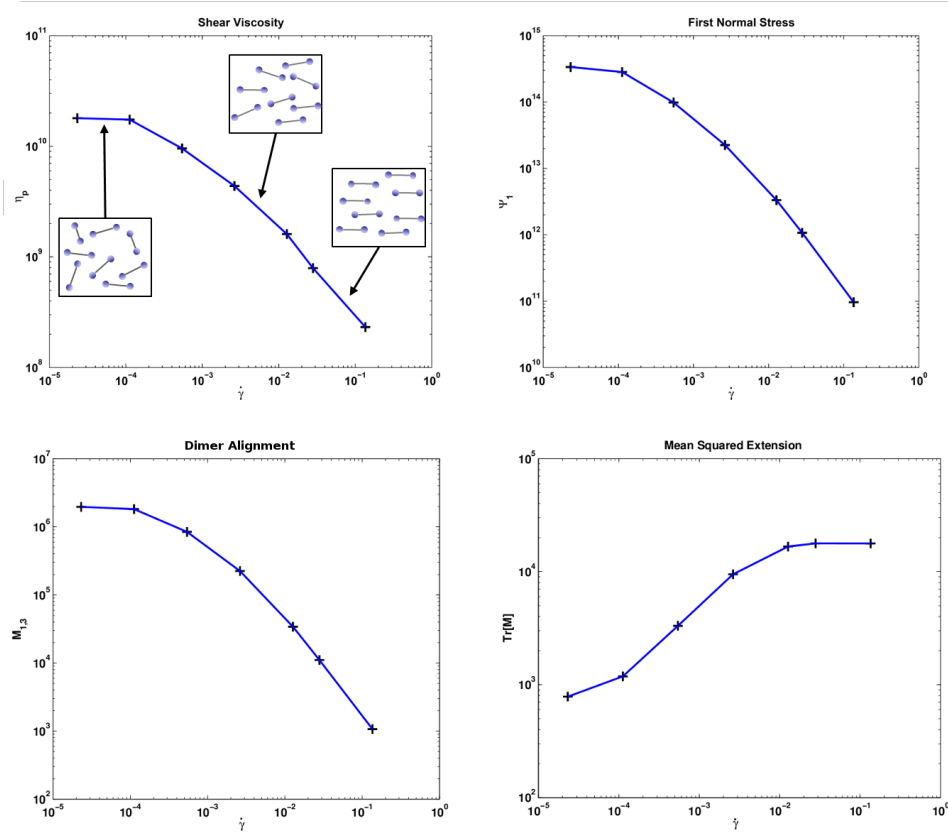
FIG. 6.1. *Polymeric Fluid Simulation Results. The shear viscosity and first normal stresses of the polymeric fluid and their dependence on the rate of shear $\dot{\gamma}$ is shown on the top left and top right. To quantitate the alignment and extension of the polymers, the orientation matrix is considered given by $M = \langle \mathbf{z}\mathbf{z}^T \rangle$, with $\mathbf{z} = \mathbf{X}^{(2)} - \mathbf{X}^{(1)}$. The component $M_{1,3}$ gives a measure of the alignment of the polymers with the direction of shear and is shown on the left. The trace of M gives a measure of the extension of the polymers and is shown on the right.*

only in the direction of the dimer orientation. As a consequence, contributions are made to the shear viscosity only when the dimer orientation has a non-negligible component in the z-direction, see equation 6.2.

The thermal fluctuations and shear stresses play opposing roles with respect to the z-component. The thermal fluctuations act to randomize the dimer orientation generating on average a non-negligible z-component while the shear stresses act to align the dimers with the direction of shear and suppress the z-component. As the shear rate increases, this results in an increase in the shear stresses and an increase in the degree of alignment of the dimers. This results in a decrease in the shear viscosity. This can be quantitated in the simulations by considering for the dimers the orientation tensor $M = \langle \mathbf{z}\mathbf{z}^T \rangle$, where $\mathbf{z} = \mathbf{X}^{(2)} - \mathbf{X}^{(1)}$, see Figure 6.1. This highlights the important roles that thermal fluctuations can play in material properties. For this polymeric fluid, if thermal fluctuations were neglected, there would be no contributions to the shear viscosity by the dimers since they would all eventually align with the direction of shear.

The observed decrease of the shear viscosity with an increase in the shear rate is a common phenomena observed for many complex fluids [9]. This behavior is referred to as "shear-thinning", see [9]. These simulations give a proof-of-principle for how such phenomena

can be studied for complex fluids using the presented computational methodology.

Parameter	Description
N	Number of mesh points in each direction.
Δx	Mesh spacing.
L	Domain size in each direction.
T	Temperature.
k_B	Boltzmann's constant.
μ	Dynamic viscosity of the solvent fluid.
ρ	Mass density of the solvent fluid.
K	Bond stiffness.
r_0	Maximum permissible bond extension.
γ_s	Stokesian drag of a particle.
$\dot{\gamma}^0$	Shear rate amplitude.
γ^0	Strain rate amplitude.
a	Effective radius of particle estimated via Stokes drag.

TABLE 6.1

Description of the parameters used in simulations of the polymeric fluid.

Parameter	Value
N	36
Δx	11.25 nm
L	405 nm
T	300 K
k_B	8.3145×10^3 nm$^2 \cdot$ amu $\cdot$ ns$^{-2} \cdot$ K^{-1}
μ	6.0221×10^5 amu $\cdot$ cm$^{-1} \cdot$ ns^{-1}
ρ	6.0221×10^2 amu $\cdot$ nm^{-3}
K	8.9796×10^3 amu $\cdot$ ns^{-2}
r_0	200 nm
γ_s	1.7027×10^8 amu $\cdot$ ns^{-1}
a	15 nm

TABLE 6.2

Values of the parameters used in simulations of the polymeric fluid.

6.2. Application II: Complex Moduli for Oscillatory Responses of Polymerized Lipid Vesicles. As a further demonstration of the computational methods, we investigate the material properties of a fluid containing polymerized lipid vesicles. We discuss how the methods can be used to study responses to an oscillatory shear applied over a wide range of frequencies.

To account for the mechanics of a polymerized lipid vesicle, we discretize the spherical surface using a triangular mesh. The mechanics is modeled by the following interactions between the control points of the mesh

$$(6.4) \qquad \phi_1(r, \ell) = \frac{1}{2} K_1 \left(r - \ell \right)^2$$

$$(6.5) \qquad \phi_2(\boldsymbol{\tau}_1, \boldsymbol{\tau}_2) = \frac{1}{2} K_1 \left| \boldsymbol{\tau}_1 - \boldsymbol{\tau}_2 \right|^2 .$$

The r denotes the displacement between two control points, ℓ denotes a preferred distance between control points, and $\boldsymbol{\tau}$ denotes a normalized displacement vector (tangent vector)
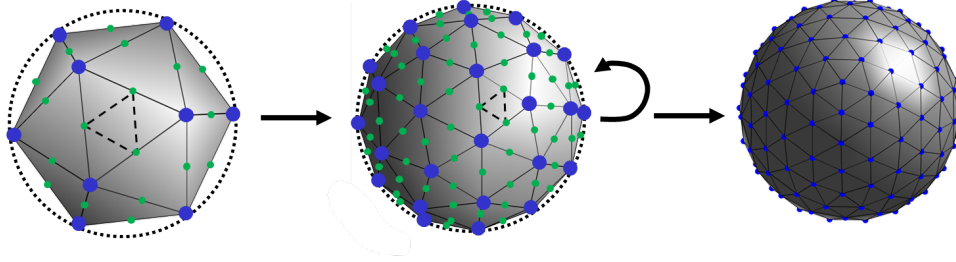
FIG. 6.2. *Vesicle Mesh Construction using a Recursive Refinement Method. The triangulated mesh for a spherical vesicle is constructed by starting with the vertices and faces of a regular icosa-hedron, shown on the left. The edges of the icosahedron are bisected and connected to divide each triangular face into four smaller triangular faces. The vertices located at the bisection points are projected radially outward to the surface of the sphere, shown in the middle. This refinement pro-cedure is repeated recursively until a mesh of sufficient resolution is obtained. The mesh obtained after two levels of recursive refinement is shown on the far right.*

between two control points. The ϕ_1 energy accounts for the stretching of a bond between two control points beyond its preferred extension. The ϕ_2 energy accounts for bending of the surface locally by penalizing the misalignment of tangent vectors. The total energy for a given configuration of the vesicle is given by

$$\Phi[\mathbf{X}] = E_1[\mathbf{X}] + E_2[\mathbf{X}] \tag{6.6}$$

$$E_1[\mathbf{X}] = \sum_{(i,j)\in\mathcal{Q}_1} \phi_1(r_{ij}, \ell_{ij}) \tag{6.7}$$

$$E_2[\mathbf{X}] = \sum_{(i,j,k)\in\mathcal{Q}_2} \phi_2(\boldsymbol{\tau}_{ij}, \boldsymbol{\tau}_{jk}). \tag{6.8}$$

The $\mathbf{X}$ denotes the composite vector of control points. The jth control point is denoted by $\mathbf{X}^{[j]}$. The $\mathcal{Q}_1$ and $\mathcal{Q}_2$ are index sets defined by the topology of the triangulated mesh.

The first energy term E_1 accounts for stretching of the vesicle surface and is computed by summing over all local two body interactions $\mathcal{Q}_1$ defined by the topology of the triangulated mesh. For the distance $r_{ij} = |\mathbf{X}^{[i]} - \mathbf{X}^{[j]}|$ between the two points having index i and j, the energy E_1 penalizes deviations from the preferred distance ℓ_{ij}. The preferred distances ℓ_{ij} are defined by the geometry of a spherical reference configuration for the vesicle. To ensure the two body interactions are represented by a unique index in $\mathcal{Q}_1$ we adopt the convention that $i < j$.

The second energy term E_2 accounts for curvature of the vesicle surface and is com-puted by summing over all local three body interactions $\mathcal{Q}_2$ defined by the topology of the triangulated mesh. The energy penalizes the the misalignment of the tangent vectors $\boldsymbol{\tau}_{ij} = (\mathbf{X}^{[i]} - \mathbf{X}^{[j]})/r_{ij}$ and $\boldsymbol{\tau}_{jk} = (\mathbf{X}^{[j]} - \mathbf{X}^{[k]})/r_{jk}$. In the set of indices in $\mathcal{Q}_2$ it is assumed that the point with index j is always adjacent to both i and k. To ensure the three body interactions are represented by a unique index in $\mathcal{Q}_2$ we adopt the convention that $i < k$.

To obtain a triangulated mesh which captures the shape of a vesicle having a spherical geometry we start with an icosahedral which is circumscribed by a sphere of a given radius. We use the faces of the icosahedron as an initial triangulated mesh. To obtain a mesh which better approximates the sphere we bisect the three edges of each triangular face to obtain four sub-triangles. The newly introduced vertices are projected radially outward to the surface of the sphere. The process is then repeated recursively to obtain further refinements of the mesh. This yields a high quality mesh for spherical geometries. We use a vesicle represented by a mesh obtained using two levels of recursive refinement. The recursive generation procedure and the mesh used to represent a vesicle is shown in Figure 6.2.
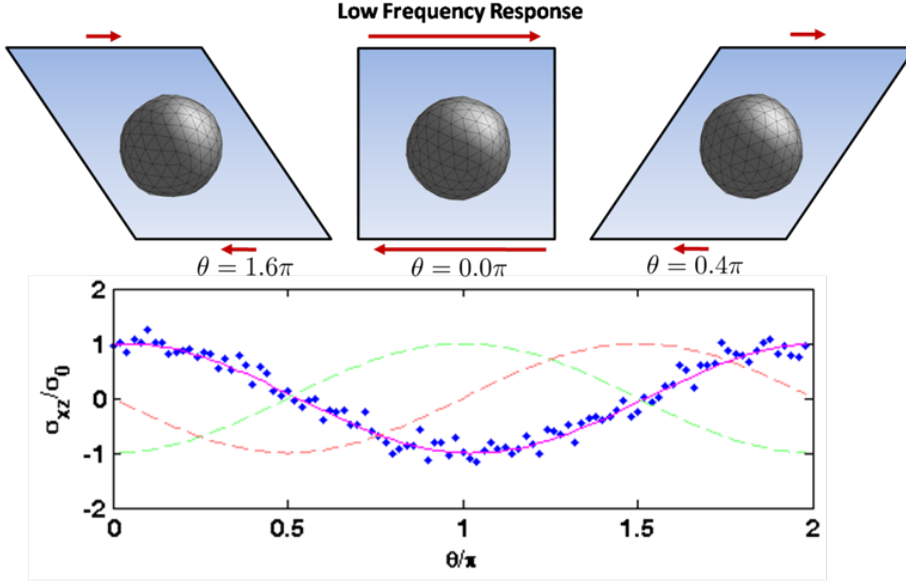
FIG. 6.3. *Polymerized Vesicle subject to Oscillatory Shear. At low frequencies the distortion of the vesicle shape is seen to be small and masked by thermal fluctuations, shown on top. The vesicle stress can be seen to follow closely the applied stress, shown at the bottom. The particular low frequency response shown corresponds to $\omega = 3.9294 \times 10^{-3} ns^{-1}$, $\dot{\gamma} = 1.9647 \times 10^{-3} ns^{-1}$, $\sigma_0 = 3.7114 \times 10^8 amu \cdot nm^{-1} \cdot ns^{-2}$.*

We investigate the response of the vesicle to oscillatory shear stresses applied with time-varying rate $\dot{\gamma} = \dot{\gamma}^0 \cos(\omega t)$. We consider a dilute regime in which it is sufficient to study a single polymerized vesicle subject to the oscillatory shear. The effective stress tensor associated with the vesicle suspension at a given time $\sigma(t)$ is estimated using the approach discussed in Section 5.

As a measure of the material response, we consider the dynamic complex modulus $G(\omega) = G'(\omega) + iG''(\omega)$, whose components are defined from measurements of the stress as the least-squares fit of the periodic stress component $\sigma_{xz}(t)$ by the function $g(t) = G'(\omega)\gamma^0 \cos(\omega t) + G''(\omega)\gamma^0 \sin(\omega t)$. This offers one characterization of the response of the material to oscillating applied shear stresses and strains as the frequency ω is varied. The G' is referred to as the Elastic Storage Modulus and G'' is referred to as the Viscous Loss Modulus. These dynamic moduli are motivated by considering the linear response of the stress components $\sigma_{xz}(t)$ to applied stresses and strains. For many materials linearity holds to a good approximation over a wide range of frequencies provided the amplitudes of the applied stresses and strains are not too large [35].

To estimate the dynamic complex modulus in practice, the least-squares fit is performed for $\sigma_{xz}(t)$ over the entire stochastic trajectory of a simulation (after some transient period). Throughout our discussion we refer to $\theta = \omega t$ as the phase of the periodic response. In our simulations, the maximum strain over each period was chosen to always be half the periodic unit cell in the x-direction, corresponding to a strain amplitude of $\gamma^0 = \frac{1}{2}$. This was achieved by adjusting the shear rate amplitude for each frequency using the expression $\dot{\gamma}^0 = \gamma^0 \omega$.

We performed simulations subjecting the vesicle to shear over a wide range of frequencies. At low frequency the distortion of the vesicle shape was found to be small and masked by thermal fluctuations when averaged over hundreds of periods. At low frequency the vesicle stresses appear to have sufficient time to equilibrate to the applied shear stresses. This is
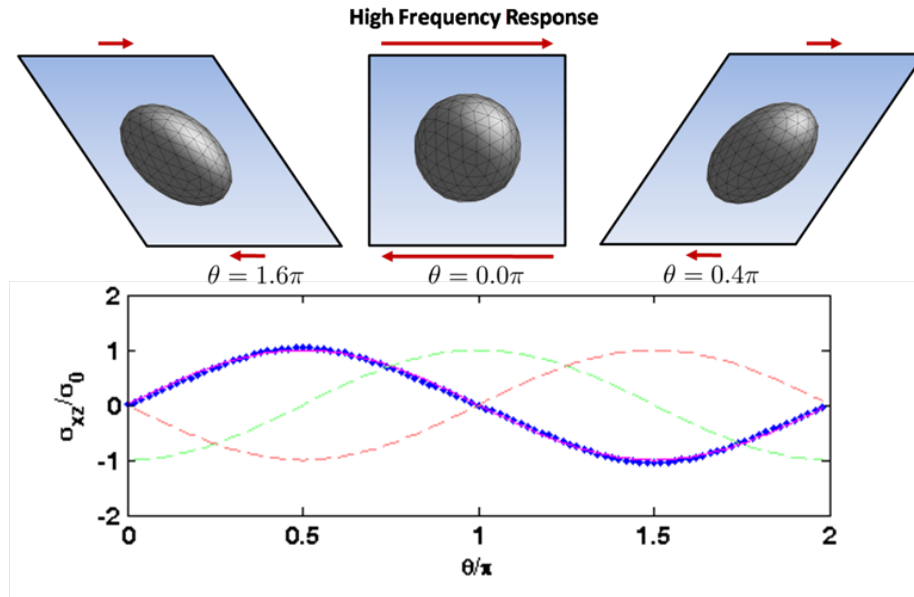
FIG. 6.4. *Polymerized Vesicle subject to Oscillatory Shear. At hight frequencies the distortion of the vesicle shape is seen to be large, shown on top. The vesicle stress can be seen to follow closely the applied strain, shown at the bottom. The particular high frequency response shown corresponds to $\omega = 1.2426 \times 10^2\, ns^{-1}$, $\dot{\gamma} = 6.2129 \times 10^1\, ns^{-1}$, $\sigma_0 = 4.6314 \times 10^{10}\, amu \cdot nm^{-1} \cdot ns^{-2}$.*

manifested in $\sigma_{xz}(t)$, which is seen to track very closely the applied stress, see Figure 6.3. At high frequencies, the vesicle shape was found to become visibly distorted and the vesicle stresses did not appear to have sufficient time to equilibrate to the applied shear stresses. These distortions can be seen in the configurations for phase $\theta = 1.6, 0.4$. The σ_{xz} is seen to be out of phase with the applied stresses but in phase with respect to the applied strain, see Figure 6.4.

These responses can be quantitated by considering the dynamic moduli. From the simulations, it is seen for the low frequency responses that the vesicle stress follows closely the applied stress. It is also found that the Viscous Loss Modulus is significantly larger than the Elastic Storage Modulus. For the high frequency response, it was found that the Elastic Storage Modulus increases and is eventually much larger than the Viscous Loss Modulus. It was also found that the Viscous Loss Modulus exhibited a non-monotonic behavior at intermediate frequencies, see Figure 6.5. A description of the parameters and specific values used in the simulations can be found in Table 6.3 and Table 6.4.
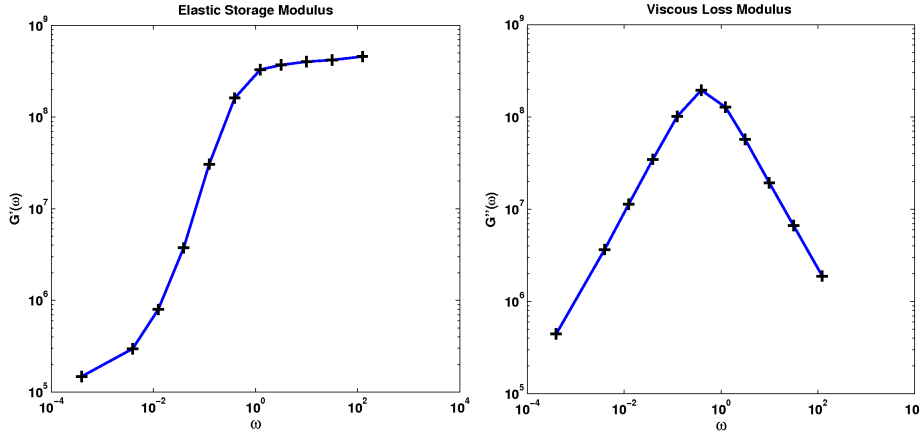
FIG. 6.5. *Frequency Response of Dynamic Moduli. The Elastic Storage Modulus $G'(\omega)$ is shown on the left and the Viscous Loss Modulus $G''(\omega)$ is shown on the right. The Viscous Loss Modulus is found to dominate at low frequency and the Elastic Storage Modulus is is found to dominate at high frequency.*

Parameter	Description
N	Number of mesh points in each direction.
Δx	Mesh spacing.
L	Domain size in each direction.
T	Temperature.
k_B	Boltzmann's constant.
μ	Dynamic viscosity of the solvent fluid.
ρ	Mass density of the solvent fluid.
K_1	Vesicle bond stiffness.
K_2	Vesicle bending stiffness.
D	Vesicle diameter.
ω	Frequency of oscillating shearing motion.
θ	Phase of the oscillatory motion, $\theta = \omega t$.
$\dot{\gamma}$	Shear rate.
$\dot{\gamma}^0$	Shear rate amplitude.
γ	Strain rate.
γ^0	Strain rate amplitude.

TABLE 6.3
Description of the parameters used in simulations of the polymerized vesicle.

Parameter	Value
N	27
Δx	7.5 nm
L	2.025×10^2 nm
T	300 K
k_B	8.3145×10^3 nm$^2 \cdot$ amu $\cdot$ ns$^{-2} \cdot$ K^{-1}
μ	6.0221×10^5 amu $\cdot$ cm$^{-1} \cdot$ ns^{-1}
ρ	6.0221×10^2 amu $\cdot$ nm^{-3}
K$_1$	2.2449×10^7 amu $\cdot$ ns^{-2}
K$_2$	8.9796×10^7
D	50 nm

TABLE 6.4

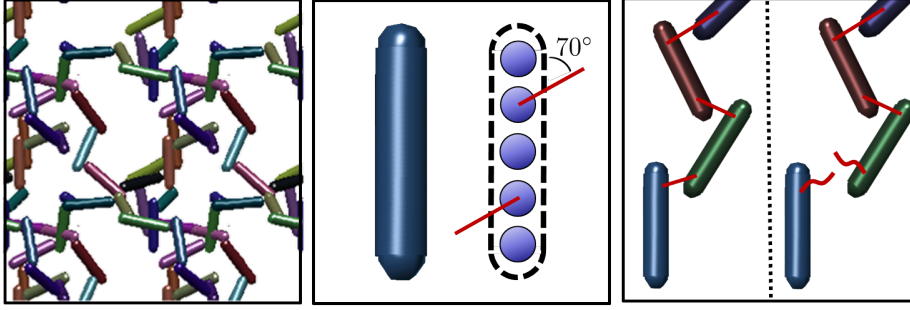*Fixed values of the parameters used in simulations of the polymerized vesicle.*

FIG. 6.6. *Microstructure of the Gel-like Material. The microstructure of the gel is comprised of polymeric chains which bind together, shown on the left. The polymeric chains are each comprised of five control points and each have specialized binding sites at the second and fourth control point, shown in the center. The inter-polymer bonds have a preferred extension and angle. When an inter-polymer bond is strained beyond 50% of its preferred rest length, the bond breaks irreversibly, shown on the right.*

6.3. Application III: Aging of the Shear Viscosity of a Gel-like Material.
As a further demonstration of how the computational methods can be used, we investigate the aging of a gel-like material subject to shear. The methods are used to study how the shear viscosity changes over time as the gel is subjected to shear at a constant rate.

The gel-like material is modeled as a collection of polymer chains which are able to bond together at two specialized sites along the chain, see Figure 6.6. The energy associated with the mechanics of the individual polymer chains and the bonds which they form are given by

$$\phi_1(r) = \frac{1}{2}K_1(r - r_{0,1})^2 \tag{6.9}$$

$$\phi_2(\boldsymbol{\tau}_1, \boldsymbol{\tau}_2) = \frac{1}{2}K_2 \left|\boldsymbol{\tau}_1 - \boldsymbol{\tau}_2\right|^2 \tag{6.10}$$

$$\phi_3(r) = \sigma^2 K_3 \exp\left[-\frac{(r - r_{0,3})^2}{2\sigma^2}\right] \tag{6.11}$$

$$\phi_4(\theta) = -K_4 \cos(\theta - \theta_{0,4}). \tag{6.12}$$

The r is the separation distance between two control points, θ is the bond angle between three control points, and $\boldsymbol{\tau}$ is a tangent vector along the polymer chain, see Figure 6.6.

The ϕ_1 energy accounts for stretching of a bond within a polymer chain from its preferred extension $r_{0,1}$. The ϕ_2 energy accounts for bending of the polymer chain locally. To account for interactions at the specialized binding sites of the polymers the potentials ϕ_3 and ϕ_4 are introduced. The potential ϕ_3 gives the energy of the bond between the two polymer chains and penalizes deviation from the preferred bond extension $r_{0,3}$. The exponential of ϕ_3 is introduced so that the resistance in the bond behaves initially like a harmonic bond but decays rapidly to zero when the bond is stretched beyond the length σ. The potential ϕ_4 gives the energy for the preferred bond angle when two of the polymer chains are bound together.

The total energy of the system is given by

$$\Phi[\mathbf{X}] = E_1[\mathbf{X}] + E_2[\mathbf{X}] + E_3[\mathbf{X}] + E_4[\mathbf{X}] \tag{6.13}$$

$$E_1[\mathbf{X}] = \sum_{(i,j)\in\mathcal{Q}_1} \phi_1(r_{ij}), \quad E_2[\mathbf{X}] = \sum_{(i,j,k)\in\mathcal{Q}_2} \phi_2(\boldsymbol{\tau}_{ij}, \boldsymbol{\tau}_{jk}) \tag{6.14}$$

$$E_3[\mathbf{X}] = \sum_{(i,j)\in\mathcal{Q}_3} \phi_3(r_{ij}), \quad E_4[\mathbf{X}] = \sum_{(i,j,k)\in\mathcal{Q}_4} \phi_4(\theta_{ijk}). \tag{6.15}$$
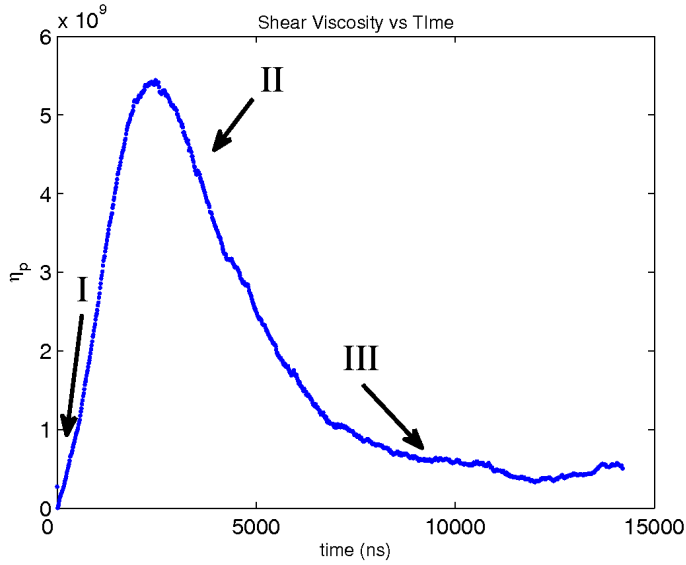
Fig. 6.7. *Aging of the Shear Viscosity Over Time. The aging of the shear viscosity exhibits roughly three stages, labeled by I, II, III. In the first stage, the gel-network maintains its integrity. Contributions to the shear viscosity arise from stretching of the inter-polymer and intra-polymer bonds. In the second stage, the inter-polymer bonds of the gel-network break. The polymers are then free to align with the direction of shear which results in relaxation of the intra-polymer bonds to their preferred rest-length. In the third stage, the contributions to the shear viscosity arise from thermal fluctuations that drive transient misalignments of the polymers with the direction of shear. These stages are each discussed in more detail in Section 6.3.*

The sets $\mathcal{Q}_k$ define the interactions according to the structure of the individual polymer chains and the topology of the gel network. When bonds are stretched beyond the critical length 3σ they are broken irreversibly, which results in the sets $\mathcal{Q}_3$ and $\mathcal{Q}_4$ being time dependent.

To study the rheological response of the gel-like material the system is subjected to shear at a constant rate. To obtain an effective macroscopic stress σ_p for the system, we use the approach from Section 5. To characterize the rheology of the gel, we consider the shear viscosity defined by

$$(6.16) \qquad\qquad \eta_p = \sigma_p^{(s,v)}/\dot{\gamma}.$$

The $\dot{\gamma}$ is the rate of the applied shear. In the notation, the superscript (s,v) indicates the tensor component with the index s corresponding to the direction of shear and the index v corresponding to the direction of shear induced velocity. The contributions of the solvent fluid to the shear viscosity are assumed to be Newtonian and can be considered separately [9].

To investigate how the shear viscosity of the gel behaves over time, multiple simulations were performed starting from an undistribed configuration of the gel network. A shear was then applied to the unit cell boundary to induce a shear deformation of the network. The shear deformation over time resulted in the breakage of bonds of the gel network. To investigate how the macroscopic material properties depend on the reorganization of the polymer chains, we considered the shear viscosity over time.

From the simulations, an interesting behavior was found. The material initially exhibited an increased shear viscosity before eventually settling down to a steady-state value. It was found that the responses of the gel-like material to shear can be roughly divided into three stages. In the first, there is an initial increase of the shear viscosity which can be attributed to
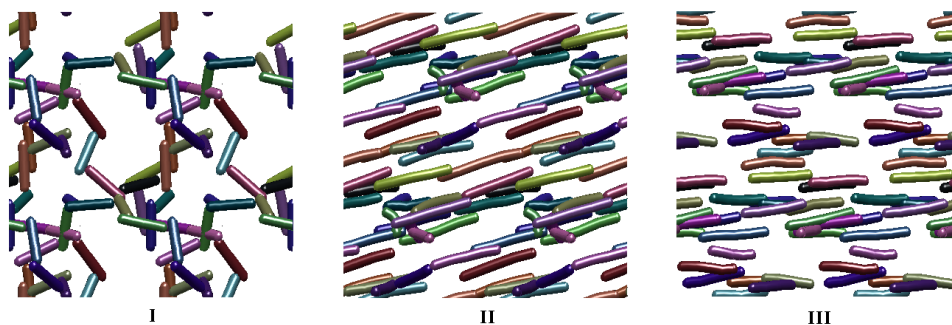
FIG. 6.8. *Microstructure Configurations for the Gel-like Material. Configurations of the microstructure are shown as the gel ages for each of the three stages discussed in Section 6.3. The times shown in these figures from left to right are $t = 0$ ns, $t = 2844$ ns, $t = 7111$ ns.*

the stretching of the inter-chain bonds between the polymer chains and the intra-chain bonds within each polymer chain. This occurs as the gel as a whole is strained for a relatively short period. The bonds between the polymer chains are observed to break with the remaining contributions to the stress arising from the shear stresses of the fluid which stretch the polymer chains. The shear viscosity in this stage and the microstructure of the gel are shown in the regions labeled by I in Figure 6.7 and Figure 6.8.

In the second stage, the individual polymer chains are seen to rotate and to start aligning with the direction of the shear. As a result of the intra-chain restoring forces the strain of the individual polymer chains is also seen to relax. The increased alignment and reduction of strain of the polymer chains yields an overall decrease in the forces transmitted in the direction of the shear gradient. Consequently, the shear viscosity begins to decrease, see the regions labeled by II in Figure 6.7 and Figure 6.8.

In the third, and last stage, the chains eventually settle into a statistical steady-state in which the thermal fluctuations drive the chains to misalign transiently with the direction of shear. These misaligned excursions by the polymer chains result on average in non-negligible forces transmitted in the direction of the shear gradient. As a consequence, the shear viscosity has a non-zero steady-state value. This is shown in the regions labeled by III in Figure 6.7 and Figure 6.8. Similar aging phenomenon is seen for many different types of soft materials and complex fluids and is often referred to as "thixotropy", see [7, 9, 13]. For the specific physical parameters used in these simulations see Table 6.5 and 6.6.

The modeling approach presented here, along with the computational methods, allow for other types of phenomena to be studied. This includes looking at the case in which the bonds between the polymer chains are able to reform. An interesting investigation in this case would be to study the kinetics and organization of the gel network when subject to both bond breaking and bond formation when the shear is greatly decreased or arrested for periods of time.

The computational methods also provide a straight-forward means to incorporate active forces operating on the filaments of the gel network. This could be useful in the study of biological materials, such as actin where motor proteins act like active cross-linkers to slide filaments past one another [12, 28, 32]. These effects could readily be taken into account in such simulations.

Parameter	Description
N	Number of mesh points in each direction.
Δx	Mesh spacing.
Δt	Time step.
L	Domain size in each direction.
T	Temperature.
k_B	Boltzmann's constant.
μ	Dynamic viscosity of the solvent fluid.
ρ	Mass density of the solvent fluid.
$\dot{\gamma}$	Shear rate.
N_p	Number of polymer chains.
N_s	Number of control points per polymer chain.
r_p	Polymer effective cylindrical radius.
K_1	Stiffness of the bonds of the polymer chain.
$r_{0,1}$	Rest length of the bonds of the polymer chain.
K_2	Bending stiffness of the polymer chain.
K_3	Stiffness of the bonds at a polymer binding site.
$r_{0,3}$	Rest length of the bond at a polymer binding site.
K_4	Bending stiffness of the bond at a polymer binding site.
$\theta_{0,4}$	Preferred angle of a bond at a polymer binding site.

TABLE 6.5

Description of the parameters used in simulations of the gel-like material.

Parameter	Value
N	72
Δx	11.25 nm
Δt	1.4222 ns
L	810 nm
T	300 K
k_B	$8.3145 \times 10^3 \text{ nm}^2 \cdot \text{amu} \cdot \text{ns}^{-2} \cdot \text{K}^{-1}$
μ	$6.0221 \times 10^5 \text{ amu} \cdot \text{cm}^{-1} \cdot \text{ns}^{-1}$
ρ	$6.0221 \times 10^2 \text{ amu} \cdot \text{nm}^{-3}$
$\dot{\gamma}$	$1.2 \times 10^{-3} \text{ ns}^{-1}$
N_p	110
N_s	5
r_p	15 nm
K_1	$2.9932 \times 10^5 \text{ amu} \cdot \text{ns}^{-2}$
$r_{0,1}$	30 nm
K_2	2.9932×10^8
K_3	$2.9932 \times 10^5 \text{ amu} \cdot \text{ns}^{-2}$
$r_{0,3}$	30 nm
K_4	2.9932×10^8
$\theta_{0,4}$	$70\,^{\circ}$

TABLE 6.6

Fixed values of the parameters used in simulations of the gel-like material.

7. Conclusions. An approach was presented for the study of complex fluids and soft materials. To study rheological responses, a specified rate of shear was imposed on the fluid and microstructures only at the boundary of the unit cell. Consistent discretizations and efficient stochastic numerical methods were developed for this formalism. To demonstrate how the approach can be used in practice, a few specific applications were presented. This included the study of shear thinning of a polymeric fluid, the study of complex moduli for the oscillatory responses of a polymerized lipid vesicle, and the study of aging of the shear viscosity of a gel-like material. The computational methods presented allow for investigations of diverse models and phenomena associated with complex fluids and soft materials. The methods allow for simulation studies which take into account the roles played by the material microstructure, elastic mechanics, hydrodynamics, and thermal fluctuations.

REFERENCES

[1] D. J. Acheson, *Elementary Fluid Dynamics*, Oxford Applied Mathematics and Computing Science Series, 1990.

[2] P.J. Atzberger, *Spatially adaptive stochastic numerical methods for intrinsic fluctuations in reaction-diffusion systems*, Journal of Computational Physics, 229 (2010), pp. 3474–3501.

[3] P. J. Atzberger, *A note on the correspondence of an immersed boundary method incorporating thermal fluctuations with stokesian-brownian dynamics*, Physica D-Nonlinear Phenomena, 226 (2007), pp. 144–150–.

[4] ——, *Stochastic eulerian lagrangian methods for fluid-structure interactions with thermal fluctuations*, (preprint), (2010). http://arxiv.org/abs/1009.5648.

[5] P. J. Atzberger and P. R. Kramer, *Error analysis of a stochastic immersed boundary method incorporating thermal fluctuations*, Mathematics and Computers in Simulation, 79 (2008), pp. 379–408–.

[6] P. J. Atzberger, P. R. Kramer, and C. S. Peskin, *A stochastic immersed boundary method for fluid-structure dynamics at microscopic length scales*, Journal of Computational Physics, 224 (2007), pp. 1255–1292–.

[7] H. A. Barnes, *Thixotropy - a review*, Journal of Non-Newtonian Fluid Mechanics, 70 (1997), pp. 1–33–.

[8] Curtiss C. F. Armstrong R. C. Hassager O. Bird, R.B., *Dynamics of Polymeric Liquids : Volume I Fluid Mechanics*, Wiley-Interscience, 1987.

[9] ——, *Dynamics of Polymeric Liquids : Volume II Kinetic Theory*, Wiley-Interscience, 1987.

[10] T. T. Bringley and C. S. Peskin, *Validation of a simple method for representing spheres and slender bodies in an immersed boundary method for stokes flow on an unbounded domain*, Journal of Computational Physics, 227 (2008), pp. 5397–5425–.

[11] P. Coussot, *Rheophysics of pastes: a review of microscopic modelling approaches*, Soft Matter, 3 (2007), pp. 528–540.

[12] Gaudenz Danuser and Clare M Waterman-Storer, *Quantitative fluorescent speckle microscopy of cytoskeleton dynamics.*, Annu Rev Biophys Biomol Struct, 35 (2006), pp. 361–387.

[13] M. Doi and S. F. Edwards, *The Theory of Polymer Dynamics*, Oxford University Press, 1986.

[14] A. Donev, E. Vanden-Eijnden, A. L. Garcia, and J. B. Bell, *On the accuracy of finite-volume schemes for fluctuating hydrodynamics*, ArXiv e-prints, 0906,2425 (2009), p. .

[15] D. J. Evans, *The frequency dependent shear viscosity of methane*, Molecular Physics, 6 (1979), pp. 1745–1754.

[16] D. J. Evans and G. P. Morriss, *Non-newtonian molecular dynamics*, Computer Physics Reports, 1 (1984), pp. 297–343.

[17] ——, *Statistical Mechanics of Non-Equilibrium Liquids*, Academic, San Diego, 1990.

[18] C. W. GARDINER, *Handbook of stochastic methods*, Series in Synergetics, Springer, 1985.

[19] G. GOMPPER AND M. SCHICK, *Soft Matter*, Wiley-VCH, 2006.

[20] D. GOTTLIEB AND S. A. ORSZAG, *Numerical Analysis of Spectral Methods Theory and Applications*, SIAM Publishing, 1993.

[21] I. W. HAMLEY, *Nanotechnology with soft materials*, Angewandte Chemie-International Edition, 42 (2003), pp. 1692–1712–.

[22] WM. G. HOOVER, CAROL G. HOOVER, AND JANKA PETRAVIC, *Simulation of two- and three-dimensional dense-fluid shear flows via nonequilibrium molecular dynamics: Comparison of time-and-space-averaged stresses from homogeneous doll's and sllod shear algorithms with those from boundary-driven shear*, Phys. Rev. E, 78 (2008), pp. 046701–14.

[23] J. H. IRVING AND JOHN G. KIRKWOOD, *The statistical mechanical theory of transport processes. iv. the equations of hydrodynamics*, J. Chem. Phys., 18 (1950), pp. 817–829.

[24] KLOEDEN.P.E. AND E. PLATEN, *Numerical solution of stochastic differential equations*, Springer-Verlag, 1992.

[25] P. R. KRAMER, C. S. PESKIN, AND P. J. ATZBERGER, *On the foundations of the stochastic immersed boundary method*, Computer Methods in Applied Mechanics and Engineering, 197 (2008), pp. 2232–2249–.

[26] R. G LARSON, *The Structure and Rheology of Complex Fluids*, Oxford University Press, 1999.

[27] A. W. LEES AND S.F. EDWARDS, *The computer study of transport processes under extreme conditions.*, J. Phys. C: Solid State Phys., 5 (1972), p. 1921.

[28] SONG LI, JUN-LIN GUAN, AND SHU CHIEN, *Biochemistry and biomechanics of cell motility.*, Annu Rev Biomed Eng, 7 (2005), pp. 105–150.

[29] E.H. LIEB AND M. LOSS, *Analysis*, American Mathematical Society, 2001.

[30] T. C. LUBENSKY, *Soft condensed matter physics*, Solid State Communications, 102 (1997), pp. 187–197–.

[31] F. MEZEI, C. PAPPAS, AND T. GUTBERLET, *Neutron spin echo spectroscopy: basics, trends, and applications*, Spinger-Verlag, 2003.

[32] DAISUKE MIZUNO, CATHERINE TARDIN, C. F. SCHMIDT, AND F. C. MACKINTOSH, *Nonequilibrium mechanics of active cytoskeletal networks.*, Science, 315 (2007), pp. 370–373.

[33] B. OKSENDAL, *Stochastic Differential Equations: An Introduction*, Springer, 2000.

[34] C. S. PESKIN, *The immersed boundary method*, Acta Numerica, 11 (2002), pp. 479–517.

[35] R. C. ARMSTRONG R. BYRON BIRD AND O. HASSAGER, *Dynamic Polymeric Liquids, Vol. I and Vol. II*, John Wiley & Sons, 1987.

[36] C. B. RAUB, V. SURESH, T. KRASIEVA, J. LYUBOVITSKY, J. D. MIH, A. J. PUTNAM, B. J. TROMBERG, AND S. C. GEORGE, *Noninvasive assessment of collagen gel microstructure and mechanics using multiphoton microscopy*, Biophysical Journal, 92 (2007), pp. 2212–2222–.

[37] L. E. REICHL, *A Modern Course in Statistical Physics*, John Wiley and Sons, 1998.

[38] G. STRANG, *Linear Algebra and its Applications*, Harcourt Brace Jovanovich College Publishers, 1988.

[39] G. STRANG AND G. FIX, *An Analysis of the Finite Element Method*, Wellesley-Cambridge Press, 2008.

[40] J. C. STRIKWERDA, *Finite Difference Schemes and Partial Differential Equations*, SIAM Publishing, 2004.

[41] L. N. TREFETHEN AND D. BAU, *Numerical Linear Algebra*, Society for Industrial and Applied Mathematics, 1997.

[42] R. B. HICKMAN A. J. C. LADD W. T. ASHURST B. MORAN W. G. HOOVER, D. J. EVANS, *Lennard-jones triple-point bulk and shear viscosities. green-kubo theory, hamiltonian mechanics, and nonequilibrium molecular dynamics*, Phys. Rev. A, 22 (1980), pp. 1690–1697.

Appendix A. A Fluctuation-Dissipation Principle for Time-Dependent Operators.

Consider the stochastic process given by

$$(A.1) \qquad d\mathbf{z}_t = L(t)\mathbf{z}_t dt + Q(t)d\mathbf{B}_t$$

$$(A.2) \qquad G(t) = QQ^T.$$

We now establish the following fluctuation-dissipation relation

$$(A.3) \qquad G(t) = -L(t)\bar{C} - \bar{C}^T L(t)^T.$$

This relates the covariance $G(t)$ of the stochastic driving field to a time-dependent dissipative operator $L(t)$ and a time-independent equilibrium covariance $\bar{C}$. We show that this relation allows for $G(t)$ to be chosen to ensure that the stochastic dynamics exhibits at statistical steady-state equilibrium fluctuations with the specified covariance $\bar{C}$.

Let the covariance at time t be denoted by

$$(A.4) \qquad C(t) = \langle \mathbf{u}(t)\mathbf{u}(t)^T \rangle.$$

By Ito's Lemma the second moment satisfies

$$(A.5) \qquad dC(t) = \Big(L(t)C(t) + C(t)^T L(t)^T + G(t)\Big)\,dt.$$

It will be convenient to express this equation by considering all of the individual entries of the matrix $C(t)$ collected into a single column vector denoted by $\mathbf{c}_t$. Similarly, for covariance matrix $G(t)$ we denote the column vector of entries by $\mathbf{g}_t$ and for $\bar{C}$ by $\bar{\mathbf{c}}$. Since the products $L(t)C(t)$ and $C(t)^T L(t)^T$ are both linear operations in the entries of the matrix $C(t)$ we can express this in terms of multiplication by of a matrix $A(t)$ acting on $\mathbf{c}_t$.

This notation allows for equation A.5 to be expressed equivalently as

$$(A.6) \qquad d\mathbf{c}_t = (A(t)\mathbf{c}_t + \mathbf{g}_t)\,dt.$$

The equation A.5 can be solved formally by the method of integrating factors to obtain

$$(A.7) \qquad \mathbf{c}_t = e^{\Xi(0,t)}\mathbf{c}_0 + \int_0^t e^{\Xi(s,t)}\mathbf{g}_s ds$$

where $\Xi(s,t) = \int_s^t A(r)dr$.

The fluctuation-dissipation relation given by equation A.3 is equivalent to choosing

$$(A.8) \qquad \mathbf{g}_s = -A(s)\bar{\mathbf{c}}.$$

For this choice, a useful identity is

$$(A.9) \qquad e^{\Xi(s,t)}\mathbf{g}_s = \frac{\partial}{\partial s}e^{\Xi(s,t)}\bar{\mathbf{c}}.$$

Substitution into equation A.7 gives

$$(A.10) \qquad \mathbf{c}_t = e^{\Xi(0,t)}\mathbf{c}_0 + \Big(e^{\Xi(t,t)} - e^{\Xi(0,t)}\Big)\bar{\mathbf{c}}.$$

Now, if $L(t)$ is negative definite uniformly in time, $\mathbf{v}^T L(t)\mathbf{v} < \alpha_0 < 0$, then $A(t)$ is also uniformly negative definite. This implies that

$$(A.11) \qquad \lim_{t\to\infty} e^{\Xi(0,t)} = 0.$$

Taking the limit of both sides of equation A.10 and using equation A.11 yields

$$(A.12) \qquad \lim_{t\to\infty} \mathbf{c}_t = \bar{\mathbf{c}}.$$

This shows that the stochastic driving field with covariance given by equation A.3 yields equilibrium fluctuations with covariance $\bar{C}$. This extends the fluctuation-dissipation relation to the case of time-dependent operators.

Appendix B. Kernel Function δ_a. We utilize a similar kernel function to the one which was used in the Stochastic Immersed Boundary Method to represent structures [6, 34].

This is given by

$$
(B.1) \qquad \phi(r) = \begin{cases}
0 & \text{, if } r \leq -2 \\[1mm]
\frac{1}{8}\left(5 + 2r - \sqrt{-7 - 12r - 4r^2}\right) & \text{, if } -2 \leq r \leq -1 \\[1mm]
\frac{1}{8}\left(3 + 2r + \sqrt{1 - 4r - 4r^2}\right) & \text{, if } -1 \leq r \leq 0 \\[1mm]
\frac{1}{8}\left(3 - 2r + \sqrt{1 + 4r - 4r^2}\right) & \text{, if } 0 \leq r \leq 1 \\[1mm]
\frac{1}{8}\left(5 - 2r - \sqrt{-7 + 12r - 4r^2}\right) & \text{, if } 1 \leq r \leq 2 \\[1mm]
0 & \text{, if } 2 \leq r.
\end{cases}
$$

For three dimensional systems the function δ_a is given by

$$
(B.2) \qquad \delta_a(\mathbf{r}) = \frac{1}{a^3} \phi\left(\frac{\mathbf{r}^{(1)}}{a}\right) \phi\left(\frac{\mathbf{r}^{(2)}}{a}\right) \phi\left(\frac{\mathbf{r}^{(3)}}{a}\right),
$$

where the superscript indicates the index of the vector component. To maintain good numerical properties, the particles are restricted to sizes $a = n\Delta x$, where n is a positive integer. For a derivation and a detailed discussion of the properties of this kernel function, see [34, 6, 10].

Appendix C. Table.

Parameter	Description
N_A	Avogadro's number.
amu	Atomic mass unit.
nm	Nanometer.
ns	Nanosecond.
k_B	Boltzmann's Constant.
T	Temperature.
η	Dynamic viscosity of water.
$\gamma_s = 6\pi\eta R$	Stokes' drag of a spherical particle.

Parameter	Value
N_A	$6.02214199 \times 10^{23}$.
amu	$1/10^3 N_A$ kg.
nm	10^{-9} m.
ns	10^{-9} s.
k_B	8.31447×10^3 amu nm^2/ns^2 K.
T	300K.
η	6.02214199 amu/cm ns.